

Interplay between exchange split Dirac and Rashba-type surface states in MnBi₂Te₄/BiTeI interface

N.L. Zaitsev

Institute of Molecule and Crystal Physics, Ufa Research Center of Russian Academy of Sciences, 450075, Ufa, Russia

I. P. Rusinov and T. V. Menshchikova
Tomsk State University, 634050 Tomsk, Russia

E. V. Chulkov

Saint Petersburg State University, 198504 Saint Petersburg, Russia

Departamento de Polímeros y Materiales Avanzados: Física, Química y Tecnología,

Facultad de Ciencias Químicas, Universidad del País Vasco UPV/EHU,

20080 Donostia-San Sebastián, Basque Country, Spain

Donostia International Physics Center (DIPC), 20018 Donostia-San Sebastián, Basque Country, Spain and

Tomsk State University, 634050 Tomsk, Russia

Based on the *ab initio* calculations, we study the electronic structure of the BiTeI/MnBi₂Te₄ heterostructure interface composed of the anti-ferromagnetic topological insulator MnBi₂Te₄ and the polar semiconductor trilayer BiTeI. We found significant difference in electronic properties at different types of contact between substrate and the overlayer. While the case of Te-Te interface forms natural expansion of the substrate, when Dirac cone state locates mostly in the polar overlayer region and undergoes slight exchange splitting, Te-I contact is the source of four-band state contributed by the substrate Dirac cone and Rashba-type state of the polar trilayer. Owing to magnetic proximity, the pair of Kramers degeneracies for this state are lifted, what produces Hall response in transport regime. We believe, our findings provide new opportunities to construct novel type spintronic devices.

I. INTRODUCTION

Interplay between spin-orbit interaction and magnetism attracts a lot of attention owing to the impact on band topology and electron transport phenomena [1–3]. In the case of asymmetric bulk and surface systems, the spin-orbit effects produce Rashba spin splitting of bulk and surface bands [4, 5], what is exploited in proposed spin-field transistor [6, 7]. Another example is quantum spin Hall effect reflected in the formation of Dirac cone states with “spin filtering” transport property on the boundaries of topological insulators (TIs) [8]. Introduction of magnetism enriches the complexity and noteworthy of the systems with mentioned spin-orbital phenomena via the breaking time-reversal symmetry and thus lifting degeneracies of Rashba states and Dirac cones. It forms additional topological band gap what is the source of spin-based transport phenomena like recently proposed chiral orbital magnetization effect [9], what allows applying such systems in spintronic devices [7, 10, 11] and quantum computation [12, 13].

One possible strategy of further research of interrelation between magnetic and spin-orbit effects is based on the design of complex heterostructures with both these contributions. Owing to the weak chemical interaction between building blocks, the van der Waals compounds provide a suitable platform to design the systems with desired properties [14, 15] via the employing molecular beam epitaxy or mechanical exfoliation techniques [16].

The ideal ingredients for design of complex heterostructures with both magnetic and spin-orbital effects

are antiferromagnetic topological insulator MnBi₂Te₄ and polar semiconductor BiTeI. The former is magnetic semiconductor [17] composed of seven layer (7L) blocks coupled by Van der Waals forces along the [0001] direction. This magnetic topological insulator has been proposed as efficient platform for magnetic spintronics [18, 19], containing exchange split bands on the (0001) cleavage plane and providing effect of magnetic proximity. Another constituent, the polar semiconductor BiTeI, is built up by polar trilayers, and is characterized by giant Rashba-type spin splitting of both bulk gap edge states and surface state [20, 21]. Excellent matching of in-plane crystal cell parameters for both constituents prevents dislocations or Moiré pattern effects during formation of the interface.

Here, we report a density functional theory (DFT) study of the van der Waals heterostructure composed by antiferromagnetic topological insulator MnBi₂Te₄(0001) surface (MBT) and polar semiconductor BiTeI trilayer resulting in formation of BiTeI/MBT interface. The Te-Te contact case forms non-magnetic extension of MnBi₂Te₄ pristine surface by BiTeI trilayer, what is expressed in spatial shifting of exchange splitted Dirac cone surface state into the overlayer region. This behavior is caused by strong spin-orbit contribution both in substrate and overlayer, and by the absence of strong perturbation of electrostatic potential over BiTeI trilayer deposition. Also it is accompanied by the shrinking of the exchange band gap of the Dirac cone and its downward shifting at overlayer deposition.

In the case of Te-I contact, the energy spectrum near

the Fermi level is formed by four-band state composed by Rashba-type state of the overlayer and Dirac state of the magnetic substrate surface. In the vicinity of the Brillouin zone center, there are two types of features: 1) hybridized band gap, owing to interaction of these two states, and 2) two exchange gaps, owing to magnetic proximity with the substrate. The latter features are the source of intrinsic Hall conductivity, due to time-reversal symmetry breaking, what allows applying this state in spintronic devices. This finding demonstrates another way to form hybridization gap between Rashba-type state and Dirac cone state, which also previously observed in pristine MBT [22] and $\text{MnBi}_6\text{Te}_{10}$ [23] surfaces.

II. CALCULATION DETAILS

The crystal structure of MnBi_2Te_4 is characterized by lattice parameters $a = 4.33 \text{ \AA}$ and $c = 40.93 \text{ \AA}$ [24]. The same a parameter is used for BiTeI trilayer placed on top of MBT (Fig. 1a). The semi-infinite MBT was represented by periodically repeated slabs of 6 septuple layers in width, with vacuum imposed in z direction along surface normal. The parallel and antiparallel aligning of the $\text{MnBi}_2\text{Te}_4(0001)$ surface normal with the BiTeI trilayer dipole moment (directed towards the Te layer) was considered. Hereinafter, we denote these two cases as Te-I and Te-Te interfaces (see Fig. 1a). We considered type of junction between the substrate and the overlayer which is similar to one of between adjacent seven-layer blocks inside the MBT substrate.

The equilibrium vertical separation d_0 between MBT and trilayer was determined from relaxation of interlayer distances of the first MBT septuple layer along with BiTeI, whereas the rest of the slab was fixed in bulk geometry. The structural optimization was performed within the PBE-D3 scheme [25, 26], which incorporates an empirical correction to include dispersion forces on top of the PBE functional using the projector augmented-wave (PAW) method [27, 28] implemented in VASP [29]. The Hamiltonian contained scalar relativistic corrections, and the spin-orbit coupling (SOC) was taken into account by the second variation method [30]. Note, that influence of spin-orbit coupling on force field is quite noticeable. The elongation of the equilibrium vertical separation d_0 due to SOC reaches 0.1 \AA in case of the Te-I interface providing $d_0 = 2.98 \text{ \AA}$, while it is half as much for the Te-Te case with $d_0 = 2.64 \text{ \AA}$.

Ab initio electronic structure calculations were performed within the DFT as implemented in the OpenMX (version 3.8) code [31]. The linear combination of localized pseudoatomic orbitals [32–34] was used to construct the basis functions. The norm-conserving pseudopotential [35] was taken as a replacement for deep core potential. The generalized gradient approximation Perdew-Burke-Ernzerhof (PBE) functional [36] was applied for the exchange-correlation energy. The basis functions

were set as follows: $\text{Mn}6.0\text{-}s3p3d2$, $\text{Te}(I)7.0\text{-}s3p3d2f1$ and $\text{Bi}8.0\text{-}s3p3d2f1$, namely, 3 primitive orbitals for each s and p channels and 2 primitive orbital for the d channel with the cutoff radius of 6.0 a.u. were used to define Mn atoms etc. The real-space grid for numerical integration and solution of the Poisson equation was set to 200 Ry of the cutoff energy. The total-energy convergence criterion was $3 \cdot 10^{-5} \text{ eV}$. The surface Brillouin zone (SBZ) of the supercell was sampled with a 7×7 mesh of \mathbf{k} points.

The calculated in-plane spin-resolved band structure of BiTeI/MBT interface with 12 \AA separation between the MBT surface and the BiTeI trilayer (to eliminate any interactions between them) is shown on Fig. 1b, c. The panels depict the bands localized within the surface septuple layer of MBT (Fig. 1b) and within the BiTeI trilayer (Fig. 1c), respectively. In contrast to the non-magnetic case of the structurally similar PbBi_2Te_4 and PbSb_2Te_4 surfaces, where Kramers degeneracies are located within the projected band gap [37, 38], the presence of a magnetic exchange field of MBT lifts this degeneracy in topological surface states (TSS) what forms the gap of $\sim 80 \text{ meV}$ (Fig. 1b). Thus, the upper part of the Dirac cone lies within the projected band gap above the Fermi level, whereas the lower part with a flattened vertex resides just above the valence band [17, 39]. Note, that at energy of $\sim -0.65 \text{ eV}$, there are trivial surface states (SS) of MBT (Fig. 1b) which are heavily involved into interaction with BiTeI, as will be seen further. In turn, the degenerate point of highly split Rashba state of BiTeI trilayer lies above the Fermi level and moreover overlaps with the bulk projected bands of MBT (Fig. 1c).

III. RESULTS

The relaxed Te-Te and Te-I interfaces have similar values of total energy, where the first one is 0.1 eV more favorable than the second one. Also, the first interface is characterized by the $\sim 0.3 \text{ \AA}$ shorter interlayer distance between trilayer and MBT (Te-Te interface spacing — $d_0 = 2.64 \text{ \AA}$, Te-I — $d_0 = 2.98 \text{ \AA}$) and is a bit shorter than vdW spacing of MBT substrate ($d_{vdW} = 2.725 \text{ \AA}$) [see also Fig. 1a]. The other inter-plane distances are tolerant to the interface type.

Ab-initio spin-resolved surface electronic spectrum of Te-Te interface (Fig. 1d) has notable changes with respect to the pristine MBT surface (Fig. 1b) and non-magnetic BiTeI/ PbSb_2Te_4 interface with the same layer stacking [37]. Namely, the tiny exchange Dirac gap (see green rectangle on Fig. 1d) of a few meV width takes place, locates just above the valence band maximum. The shifted down Dirac state has increased velocity. With that, at the SBZ center the lower part of the Dirac cone overlaps with the set of weak surface states inherited from the highest MBT bulk valence state, due to electrostatic field near the surface. In turn, the Rashba-type state resides at energy of $\sim 0.2 \text{ eV}$ lessening their momentum splitting. Note, that BiTeI overlayer on MBT

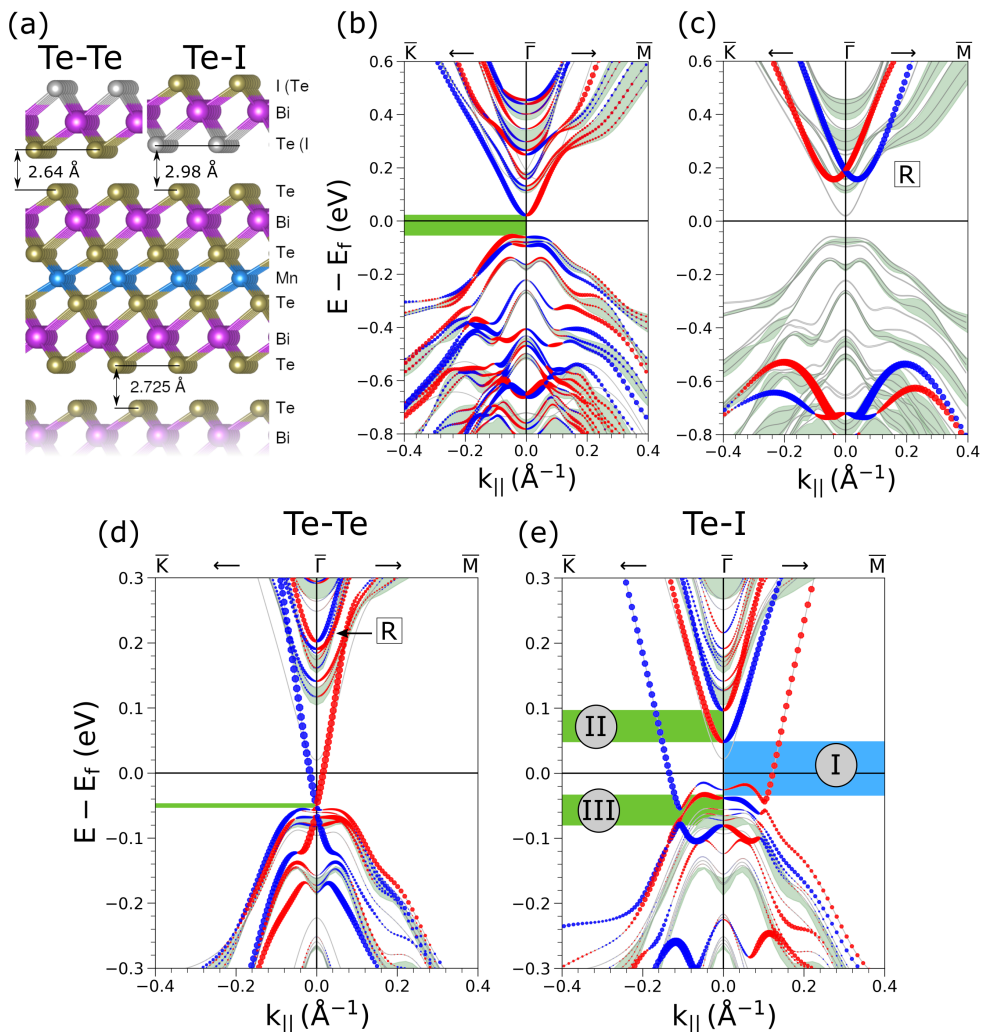


Figure 1. (a) Schematic geometrical structure of the BiTeI/MBT interface with different orientations of BiTeI trilayer. *In-plane* spin-resolved band structure calculated with large separation of 12 Å between (b) pristine MnBi₂Te₄(0001) surface and (c) BiTeI trilayer. Spin-resolved electron spectrum for (d) Te-Te and (e) Te-I interfaces in the case of equilibrium structures. The value and direction of *in-plane* spin projection are coded by circle size and color (red and blue). The gray area represents bulk projected bands, and the black rectangular emphasizes the trivial surface states of MnBi₂Te₄(0001). For panels (b), (d) and (e), the magnetic exchange and hybridization energy gap at the center of SBZ are denoted by green (blue) rectangles. In panel (e), the hybridization energy gap is denoted as I, and two exchange gaps — as II and III. In panels (c) and (d), the unoccupied Rashba state are denoted by R symbol.

prone to pull the surface states into itself, like in the case of adsorption on Au(111) [40] or PbSb₂Te₄(0001) [37] surfaces.

The another trends can be seen in electronic structure of Te-I interface (see Fig. 1 e). In the area near the Fermi level the set of spin-polarized states appears. As will be discussed afterwards in detail, they are separated by energy gaps of different nature. The two gaps (II and III) [green color rectangles] are of exchange type and are originated from the presence of magnetic MBT substrate. The highest (lowest) exchange gap is of ~ 49 meV (of ~ 42 meV) width. Another type gap (I) is crossed by the Fermi level and is of ~ 86 meV

width (blue color rectangle). It has hybridization character and is induced by interaction of the surface cone state of MBT and the Rashba-type state of the overlayer. The gap of same nature has been observed previously at consideration of non-magnetic BiTeI/PbSb₂Te₄ surface heterostructure [37]. In such a way, Te-I interface forms single four-band state composed of two-band Dirac and Rashba-type states. Out of the area of the SBZ center, where hybridization gap is formed, the discussed four-band state dispersion is inherited from these spin-orbit contributions, separately. It should be noted, that due to presence of the valence band maximum which plays a role of charge reservoir, the potential gradient near

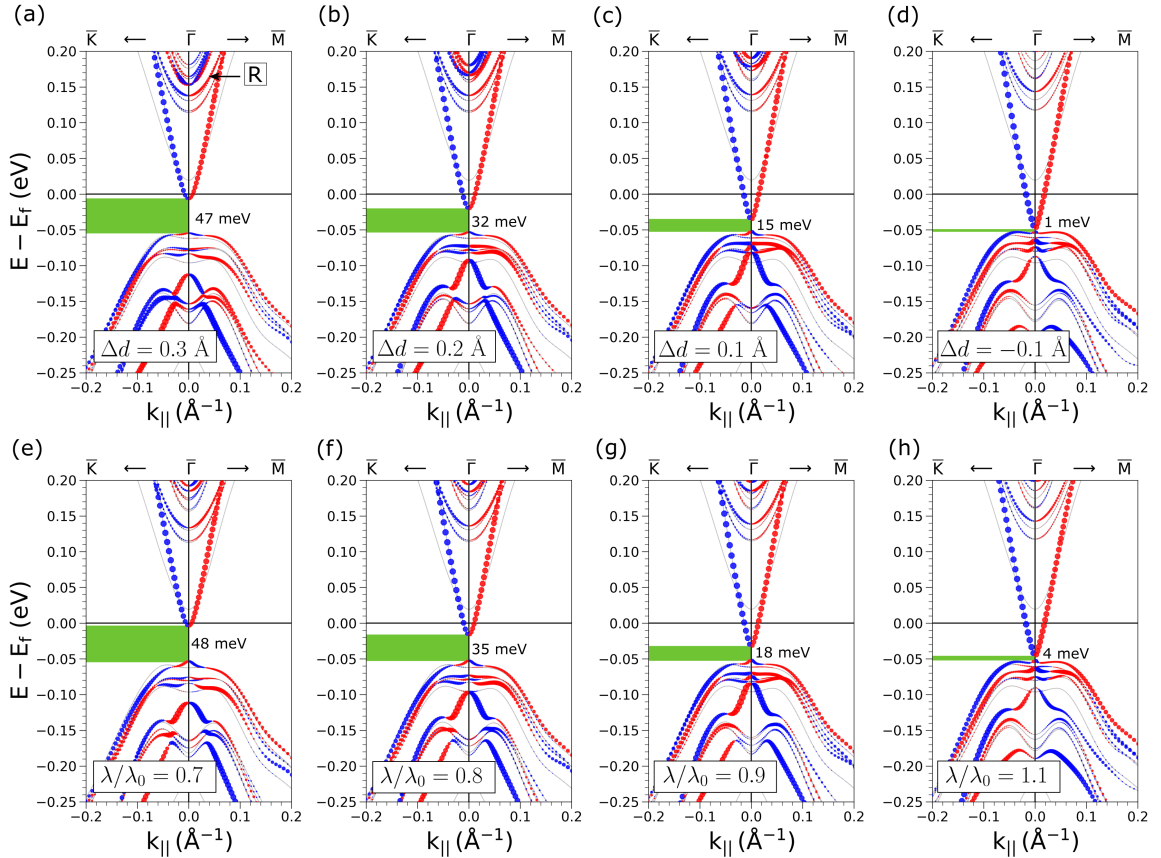


Figure 2. Surface spin-resolved electronic structure of Te-Te interface (a-d) for different separations between the MBT surface and trilayer with respect to equilibrium geometry, $\Delta d = d - d_0$, and (e-h) for different spin-orbit coupling strength of Bi and Te p -states of BiTeI trilayer. The natural SOC contribution gives $\lambda/\lambda_0 = 1$. On the panels, magnetic exchange gap at SBZ center are reflected by green areas. For each panel, the gap width is denoted from the right side of the green area. In panel (a), the subsurface Rashba state is denoted by R symbol.

the surface region produces the additional surface states which are involved into the interaction with four-band state under consideration, which can be regarded as simplification of low-energy surface electronic spectrum for this type of interface.

Te-Te interface

The origins of the calculated electronic structure of the equilibrium Te-Te interface can be clarified by varying the vertical separation, d , between MBT and polar trilayer what changes interaction between these building blocks. Also, electronic spectra at increased d correspond to the cases of additional intercalated atoms into the van der Waals region [41–43]. At $d=4$ Å, the interaction between substrate and overlayer is weak, and the bands alignment has no substantial changes with respect to fully decoupled case presented on the Fig. 1 c. However, this weak interaction induces notable ~ 0.3 eV upward shift of Rashba-type surface states. The decrease-

ing distance d reduces the Rashba-type splitting of bands and enforces the mentioned energy shift accompanied by charge density relocation into the upper septuple block of the MBT substrate. When the spacing increases and becomes to be of 0.3 Å greater than the equilibrium one ($\Delta d = d - d_0 = 0.3$ Å), the former Rashba state diminishes surface character and completely declines their momentum splitting (see Fig. 2 a). Herewith, in the area of Fermi level the exchange gap of the Dirac states reduces owing to down energy shift of the upper part of the cone, and the apex of lower part lies at energy of -0.11 eV at the Γ -point. At further reduction of d , the formation of almost gapless Dirac state is revealed which is hybridized with the bulk bands near the SBZ center forming set of surface resonances (Fig. 2 c). The minimal gap is observed at equilibrium distance, $d = d_0$, (Fig. 1 d). The subsequent shrinking of the interlayer distance, d , shifts the topological surface states down in the energy scale (Fig. 2d), albeit the exchange gap size is still negligible. Note, that the TSS wave function tends to be localized in the trilayer when approaching to MBT similar to the case of

BiTeI/Au(111) interface [40]. However, under further reducing d the TSS pulls back to the MBT surface (Fig. 3) due to the proximity of the TSS and the highest valence bulk states continuum what produces the resonant character of TSS in the energy area near the exchange gap.

The distance dependent surface electronic structure evolves in a similar way as it happens at artificial SOC modulation on Bi and Te atoms of the trilayer (see Fig. 2). At increasing interlayer distance by $\Delta d = 0.1 \text{ \AA}$, surface states shift in a similar fashion as at reducing the SOC factor by 10%, $\lambda/\lambda_0 = 0.9$ (Fig. 2 c,g). Note, that it is enough to modulate SOC factor of p -states only, since the TSS are predominantly composed by this type of orbitals. Again, under compression, $\Delta d = -0.1 \text{ \AA}$, (Fig. 2 d) or, otherwise, at increased SOC factor, $\lambda/\lambda_0 = 1.1$, the lower part of the cone shifts down in the energy scale (Fig. 2 h). Moreover, the wave function of the upper part of cone is maximally localized on the trilayer at equilibrium distance and natural SOC contribution, $\lambda/\lambda_0 = 1$. With increasing λ/λ_0 , the Dirac cone charge localization is extruded back to the MBT in the same way as at approaching BiTeI trilayer close to MBT surface (Fig. 3).

The effect described just above is originated by antiparallel directed trilayer dipole moment which induces a potential gradient on the MBT surface. The same has been previously observed under additional surface doping [39] when the surface negative charge reduces the exchange gap in pristine MBT [39], due to downshift of the upper part of the split Dirac cone. Such relationship of spin-orbit interaction and electric field effects has been revealed in various materials [44–46].

For this type termination, the formation of the exchange gap in the Dirac state is the source of the range of transport phenomena: half-quantized Hall conductivity[47], anomalous Hall effect[48, 49] and topological magnetoelectric effect[50, 51].

Te–I interface

The inverted polarity of the trilayer in the Te-I interface leads to the parallel orientation of the dipole moment of this building block with respect to the MBT surface normal. It provides the positive potential gradient near the vacuum region. Hence, at approaching of the trilayer closer to the MBT surface the Dirac state reallocates inside the trilayer. Such an effect of TSS redistribution towards the vacuum boundary has been previously observed in the case of MBT surfaces under the positive external electric field [39]. Also, in the case of the Te-I interface over the Δd decreasing the Rashba-type state moves down in the spectrum. In such a way, at $\Delta d = 1 \text{ \AA}$, this state overlaps with the lower part of the Dirac cone immediately below the Fermi level with the formation of hybridization between them. It manifests the single four-band composite state persisted at subsequent decreasing of Δd .

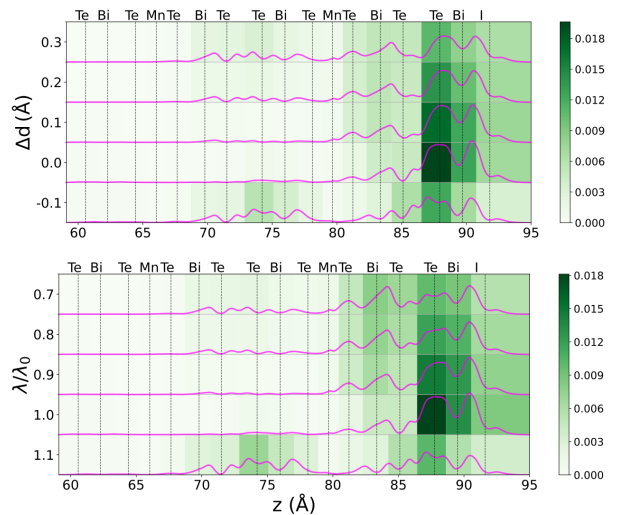


Figure 3. Te-Te interface: charge density distribution of the upper part of the Dirac surface state (purple curves) at the $\bar{\Gamma}$ -point as function of out-of-plane direction (integrated over xy -plane) for different vertical spacing between the MBT surface and trilayer (top panel) and spin-orbit coupling strength, λ/λ_0 (bottom panel) [see also Fig. 2]. The integral of charge density inside the vicinity of adjoined atomic layers are color-coded by intensities of green.

In Fig. 4 a, the corresponding spectra are shown for $\Delta d = 0.3 \text{ \AA}$ (left panel) and $\Delta d = -0.1 \text{ \AA}$ (right panel). The approaching the trilayer closer to the MBT surface affects the width of local band gaps of different nature. Over this process, the hybridization gap (marked as I on the figure) is becoming larger (from 57 meV at $\Delta d = 0.3 \text{ \AA}$, up to 100 meV at $\Delta d = -0.1 \text{ \AA}$), what agrees with enhancing the interaction between building blocks. At the same time, local exchange gaps (II, III) behave differently. The unoccupied one is shrinking from 52 meV ($\Delta d = 0.3 \text{ \AA}$) to 45 meV ($\Delta d = -0.1 \text{ \AA}$), while the occupied one, on the contrary, enlarges from 34 meV to 46 meV. Such an effect says for the complexity of the interaction between hybridization and exchange contribution for this four-band state. Another effect of the complex hybridization of Rashba-type and Dirac states is expressed in spectra by changing the character of the contribution in the vicinity of the $\bar{\Gamma}$ -point for the hybridization gap edges. The unoccupied branch is composed by the Dirac state contribution what corresponds to the localization within the two upper SL blocks (2SL), while the occupied one is formed by the Rashba-type contribution (localized within the trilayer block). Out of the SBZ center, the contribution becomes inverted, i.e. unoccupied band is contributed by the trilayer block, while the occupied one — by the 2SL blocks.

To address the transport properties of the composite four-band surface state at Te-I interface, we use the simple $\mathbf{k}\mathbf{p}$ -model. The model Hamiltonian (eq. 1) is composed by two contributions. The first one describes the

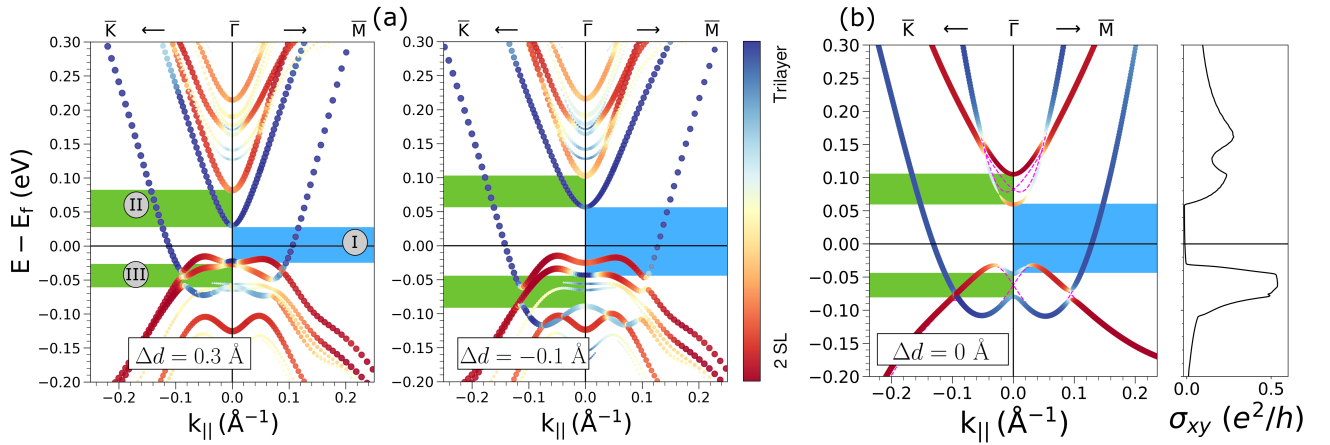


Figure 4. (a) Surface electronic structure of the Te-I interface for different spacings between the BiTeI overlayer and MBT surface. The spacing is 0.3 \AA greater (left panel) and 0.1 \AA lesser (right panel) than the equilibrium one. The colors highlight the extent of spacial localization of the states inside the trilayer (blue) or within the two utmost septuple layers of MBT (red). (b) Electronic band structure (eq. 1) of proposed model (left panel) with parameters tabulated in Table I (solid black lines), and without taken into account magnetic contribution, \hat{H}_m ($\Delta_R = \Delta_D = 0$) (dashed red lines). (Right panel) Energy dependence of Hall conductivity $\sigma_{xy}(E) = V/(2\pi)^2 \int d^2\mathbf{k} \sigma_{xy}(\mathbf{k}, E)$. For all panels, the magnetic exchange and hybridization energy gap at the center of SBZ are denoted by green (blue) areas. Hybridization energy gap is denoted as I, and two exchange gaps — as II and III.

linear Dirac-type states and Rashba-type states interaction, second one — time-reversal symmetry breaking magnetic contribution, \hat{H}_m :

$$\hat{H}(\mathbf{k}) = \begin{pmatrix} \hat{H}^D(\mathbf{k}) & \hat{H}_{int} \\ \hat{H}_{int}^\dagger & \hat{H}^R(\mathbf{k}) \end{pmatrix} - \hat{H}_m. \quad (1)$$

Here, $\hat{H}^D(\mathbf{k})$ and $\hat{H}^R(\mathbf{k})$ are 2×2 Hamiltonians of the Dirac and Rashba-type states localized in the uppermost seven-layer block of the substrate and BTI overlayer, respectively. Both the contributions have the same form, distinguishing by parameter values:

$$\hat{H}^\mu(\mathbf{k}) = M_0^\mu + M_1^\mu k^2 + \alpha_\mu (k_x \hat{\sigma}_y - k_y \hat{\sigma}_x) + \frac{\gamma_\mu}{2} (k_+^3 + k_-^3) \hat{\sigma}_z,$$

where $\hat{\sigma}$ are Pauli matrices in spin space, μ identifies the Dirac (D) or Rashba (R) part of the Hamiltonian, M_0^μ and M_1^μ are constant-energy shift and kinetic energy strength contribution, respectively. α_μ and γ_μ are spin-orbit and hexagonal warping strength, respectively[52]. Hybridization contribution, \hat{H}_{int} , does not depend on momentum and takes the form $A\sigma_0$. Magnetic term is defined by $\hat{H}_m = \text{diag}(\Delta_D, -\Delta_D, \Delta_R, -\Delta_R)$, where Δ_μ is the strength of Zeeman contribution with out-of-plane magnetic moment. It should be noted that the proposed model is relevant within the small area near the $\bar{\Gamma}$ -point, where possible higher-order terms are caused by the impact of another nearby surface and resonant states. The parameters of the Hamiltonian have been obtained via the fitting procedure applied to *ab-initio* surface spectrum, and are shown in the Table I. The Rashba-type

part, $\hat{H}^R(\mathbf{k})$, has dominant kinetic energy term, M_1^R , with respect to the spin-orbit contribution strength, α_R , and has opposite sign with respect to the one of $H_D(\mathbf{k})$. The relative difference between exchange parameters Δ_R and Δ_D ($\Delta_D/\Delta_R = 3.5$) in the Rashba-type state and linear Dirac state is in the good accordance with aspects of localization of these states: the former is located mostly in the trilayer block, while the latter — in uppermost seven-layer block of the magnetic substrate.

On the left panel of Fig. 4 b, energy spectrum of the presented model is shown for the parameters given in the Table I (color-coded curves), and for these parameters, but without magnetic contribution, $\Delta_D = \Delta_R = 0$ (red dashed lines). The bright feature of the presented spectra is the hybridization band gap near the $\bar{\Gamma}$ -point, at -0.02 – 0.05 eV energy range (Fig. 4.a), what is formed by non-zero A , and this aspect of the model exactly reproduces *ab-initio* results. As can be seen in the figure the magnetism enhances the range of features in the spectrum. Firstly, it produces local exchange gaps in the vicinity of the $\bar{\Gamma}$ -point at ~ 0.08 eV and ~ 0.1 eV (green color on the figure), what is also in agreement with *ab-initio* results. Secondly, it is avoided crossings: at ~ 0.08 eV, they are located along $\bar{\Gamma} - \bar{K}$ direction, while along $\bar{\Gamma} - \bar{M}$ such features are also caused by additional hexagonal warping effect. At ~ 0.15 eV, the formation of this type of features is artificial, owing to limitation of $\mathbf{k}\mathbf{p}$ -model producing the intersection of Rashba-type and the linear Dirac state branches without magnetism.

Both time reversal symmetry breaking and surface inversion asymmetry induce non-zero Hall conductivity. On the right panel of Fig. 4 b, the energy dependence of

Table I. Parameters of the four-band (eq. 1), obtained from the fitting *ab-initio* band spectrum.

	$\mu = D$	$\mu = R$		$\mu = D$	$\mu = R$
M_0^μ (eV)	0.05	-0.02	α_μ (eV Å)	1.42	-1.90
M_1^μ (eV Å ²)	2.29	15.66	γ_μ (eV Å ³)	11.85	26.67
Δ_μ (eV)	0.035	0.010	A (eV)	0.06	

Hall conductivity, σ_{xy} , integrated over momentum space at each E . Hall conductivity has been calculated by using anti-symmetric component of topological Berry curvature tensor $\Omega_n^{xy}(\mathbf{k})$:

$$\sigma_{xy}(\mathbf{k}, E) = \frac{e^2}{h} \sum_n f(E_n - E) \Omega_{xy}^n(\mathbf{k}),$$

where f is Fermi function, and $\Omega_n^{xy}(\mathbf{k})$ has been computed by using Kubo formula:

$$\Omega_{xy}^n(\mathbf{k}) = 2\hbar^2 \text{Im} \sum_{n' \neq n} \frac{\langle n | \hat{v}_x | n' \rangle \langle n' | \hat{v}_y | n \rangle}{[E_n - E_{n'}]^2},$$

where velocity operators are $\hat{v}_{x,y} = 1/\hbar \partial \hat{H} / \partial k_{x,y}$.

The maximal intensity is located at energy where magnetic contribution into the band dispersion is maximal, i.e. the regions of the exchange gaps and avoided crossings. The bright peak of $\sigma_{xy}(E)$ is located at -0.08 eV, decaying down to the energy scale. At energy range of 0.08-0.18 eV, two-peak feature is shown, where the lower peak corresponds to the exchange gap at the $\bar{\Gamma}$ -point and the higher — the discussed avoided crossing feature. In such a way, there are two energy areas contributed to the Hall conductivity, and they correspond to the local band gaps of lifted Kramers degeneracies due to the magnetism.

IV. CONCLUSION

In the case of Te-side MBT/BTI, the effect of the presence of the overlayer induces spatial shift of exchange splitted Dirac cone into the region of the BiTeI overlayer and in reducing of the exchange gap size with respect to pristine surface of the substrate. As the result, the surface Dirac cone mostly locates inside the polar overlayer despite that Rashba-type spin splitting is spectral peculiarity of BiTeI compound. Such an effect is related with bulk gap edge states inversion of the substrate, what has

been also demonstrated via the *ab-initio* calculations. In such a way, the deposition of BiTeI trilayer on MnBi₂Te₄ surface can be the route to manipulation of exchange gap size of the Dirac cone.

Between two possible side surfaces of MBT/BTI interfaces, the Te-side interface case stands out by the formation of four-band state induced by Rashba-type and linear Dirac cone coupling. Owing to magnetic nature of the substrate, this state undergoes sizable exchange splitting, what ensures intrinsic Hall conductivity contribution via the time-reversal symmetry breaking. Here-with, the observed conductivity is not quantized due to non-zero density of states in the corresponded energy region. The described properties of the four-band state resemble those of widely studied exchange-split Rashba-type state which is a useful model to study fundamental aspects of anomalous Hall conductivity [11]. Hence, one can expect the same magneto-transport phenomena for the described four-band state of the current investigation. First of all, additional random impurities should produce extrinsic side-jump and skew-scattering contribution to anomalous Hall conductivity in the I-side of the MBT/BTI interface [53–55]. Next, one can expect the surface anisotropic magnetoresistance effect [56, 57]. Due to strong spin-orbit coupling contribution of BiTeI overlayer, Dzyaloshinskii-Moriya spin interaction can be produced what ensures the formation of skyrmions and magnetic domain walls [58], what opens the way for manipulation of spin momentum of electron based on recently proposed chiral orbital magnetization effect [9]. Another type of related photo-voltaic and optical effects in the proposed system are photo-current at zero bias voltage [59–61] or topological Kerr effect [62, 63]. By organization of proximity with superconductor, it can possible create Majorana fermion states [64, 65] what allows one to apply the proposed heterostructure in quantum computation [13]. We note, the considered four-band state can be more advantage with respect to the Rashba-type state, owing to the presence of two wide energy ranges with contribution of Hall conductivity. As a results, the Fermi-level can be easily pinned at this energy regions via the surface doping.

V. ACKNOWLEDGEMENTS

E.V.C. acknowledges support from Saint Petersburg State University (Grant No. ID 90383050). N.L.Z., I.P.R. and T.V.M. acknowledge support from Russian Science Foundation within Research Project No. 18-12-00169-p.

[1] T. Jungwirth, X. Marti, P. Wadley, and J. Wunderlich, Nature Nanotechnology **11**, 231 (2016), ISSN 1748-3395, URL <https://doi.org/10.1038/nnano.2016.18>. I

[2] D. N. Basov, R. D. Averitt, and D. Hsieh, Nature Materials **16**, 1077 (2017), ISSN 1476-4660, URL <https://doi.org/10.1038/nmat5017>.

- [3] Y. Tokura, K. Yasuda, and A. Tsukazaki, *Nature Reviews Physics* **1**, 126 (2019), ISSN 2522-5820, URL <https://doi.org/10.1038/s42254-018-0011-5>. I
- [4] Y. A. Bychkov and E. I. Rashba, *JETP Letters* **39**, 78 (1984). I
- [5] G. Bihlmayer, O. Rader, and R. Winkler, *New Journal of Physics* **17**, 050202 (2015). I
- [6] S. Datta and B. Das, *Applied Physics Letters* **56**, 665 (1990). I
- [7] I. Žutić, J. Fabian, and S. Das Sarma, *Rev. Mod. Phys.* **76**, 323 (2004), URL <https://link.aps.org/doi/10.1103/RevModPhys.76.323>. I
- [8] M. Z. Hasan and C. L. Kane, *Rev. Mod. Phys.* **82**, 3045 (2010), URL <https://link.aps.org/doi/10.1103/RevModPhys.82.3045>. I
- [9] F. R. Lux, F. Freimuth, S. Blügel, and Y. Mokrousov, *Communications Physics* **1**, 60 (2018), ISSN 2399-3650. I, IV
- [10] A. Manchon, J. Železný, I. M. Miron, T. Jungwirth, J. Sinova, A. Thiaville, K. Garello, and P. Gambardella, *Rev. Mod. Phys.* **91**, 035004 (2019), URL <https://link.aps.org/doi/10.1103/RevModPhys.91.035004>. I
- [11] N. Nagaosa, J. Sinova, S. Onoda, A. H. MacDonald, and N. P. Ong, *Rev. Mod. Phys.* **82**, 1539 (2010), URL <https://link.aps.org/doi/10.1103/RevModPhys.82.1539>. I, IV
- [12] S. R. Elliott and M. Franz, *Rev. Mod. Phys.* **87**, 137 (2015), URL <https://link.aps.org/doi/10.1103/RevModPhys.87.137>. I
- [13] C. Nayak, S. H. Simon, A. Stern, M. Freedman, and S. Das Sarma, *Rev. Mod. Phys.* **80**, 1083 (2008), URL <https://link.aps.org/doi/10.1103/RevModPhys.80.1083>. I, IV
- [14] A. K. Geim and I. V. Grigorieva, *Nature* **499**, 419 (2013), ISSN 1476-4687, URL <https://doi.org/10.1038/nature12385>. I
- [15] K. S. Novoselov, K. Mishchenko, A. Carvalho, and A. H. Castro Neto, *Science* **353** (2016). I
- [16] H. Qi, L. Wang, J. Sun, Y. Long, P. Hu, F. Liu, and X. He, *Crystals* **8** (2018). I
- [17] M. M. Otrokov, I. I. Klimovskikh, H. Bentmann, D. Estyunin, A. Zeugner, Z. S. Aliev, S. Gaß, A. U. B. Wolter, A. V. Koroleva, A. M. Shikin, et al., *Nature* **576**, 416 (2019), ISSN 1476-4687, URL <https://doi.org/10.1038/s41586-019-1840-9>. I, II
- [18] M. M. Otrokov, T. V. Menshchikova, M. G. Vergniory, I. P. Rusinov, A. Y. Vyazovskaya, Y. M. Koroteev, G. Bihlmayer, A. Ernst, P. M. Echenique, A. Arnau, et al., *2D Materials* **4**, 025082 (2017). I
- [19] M. M. Otrokov, I. P. Rusinov, M. Blanco-Rey, M. Hoffmann, A. Y. Vyazovskaya, S. V. Eremeev, A. Ernst, P. M. Echenique, A. Arnau, and E. V. Chulkov, *Phys. Rev. Lett.* **122**, 107202 (2019), URL <https://link.aps.org/doi/10.1103/PhysRevLett.122.107202>. I
- [20] K. Ishizaka, M. S. Bahramy, H. Murakawa, M. Sakano, T. Shimojima, T. Sonobe, K. Koizumi, S. Shin, H. Miyahara, A. Kimura, et al., *Nature Materials* **10**, 521 (2011), ISSN 1476-4660, URL <https://doi.org/10.1038/nmat3051>. I
- [21] S. V. Eremeev, I. A. Nechaev, Y. M. Koroteev, P. M. Echenique, and E. V. Chulkov, *Phys. Rev. Lett.* **108**, 246802 (2012), URL <https://link.aps.org/doi/10.1103/PhysRevLett.108.246802>. I
- [22] A. Liang, C. Chen, H. Zheng, W. Xia, K. Huang, L. Wei, H. Yang, Y. Chen, X. Zhang, X. Xu, et al., *Nano Letters* **22**, 4307 (2022), ISSN 1530-6984. I
- [23] X.-M. Ma, Z. Chen, E. F. Schwier, Y. Zhang, Y.-J. Hao, S. Kumar, R. Lu, J. Shao, Y. Jin, M. Zeng, et al., *Phys. Rev. B* **102**, 245136 (2020). I
- [24] D. S. Lee, T.-H. Kim, C.-H. Park, C.-Y. Chung, Y. S. Lim, W.-S. Seo, and H.-H. Park, *CryStEngComm* **15**, 5532 (2013), ISSN 1466-8033, URL <https://pubs.rsc.org/en/content/articlelanding/2013/ce/c3ce40643a>. II
- [25] S. Grimme, J. Antony, S. Ehrlich, and H. Krieg, *The Journal of Chemical Physics* **132**, 154104 (2010), ISSN 0021-9606, 1089-7690, URL <http://scitation.aip.org/content/aip/journal/jcp/132/15/10.1063/1.3382344>. II
- [26] S. Grimme, S. Ehrlich, and L. Goerigk, *Journal of Computational Chemistry* **32**, 1456 (2011), ISSN 01928651, URL <http://doi.wiley.com/10.1002/jcc.21759>. II
- [27] P. E. Blöchl, *Phys. Rev. B* **50**, 17953 (1994). II
- [28] G. Kresse and D. Joubert, *Phys. Rev. B* **59**, 1758 (1999). II
- [29] G. Kresse and J. Furthmüller, *Comput. Mater. Sci.* **6**, 15 (1996). II
- [30] D. D. Koelling and B. N. Harmon, *J. Phys. C: Sol. Stat Phys.* **10**, 3107 (1977). II
- [31] T. Ozaki, H. Kino, J. Yu, M. Han, N. Kobayashi, M. Ohfuti, F. Ishii, T. Ohwaki, H. Weng, and K. Terakura, <http://openmx-square.org/>. II
- [32] T. Ozaki, *Physical Review B* **67**, 155108 (2003). II
- [33] T. Ozaki and H. Kino, *Physical Review B* **69**, 195113 (2004).
- [34] T. Ozaki and H. Kino, *Physical Review B* **72**, 045121 (2005). II
- [35] N. Troullier and J. L. Martins, *Physical Review B* **43**, 1993 (1991). II
- [36] J. P. Perdew, K. Burke, and M. Ernzerhof, *Phys. Rev. Lett.* **77**, 3865 (1996). II
- [37] S. V. Eremeev, S. S. Tsirkin, I. A. Nechaev, P. M. Echenique, and E. V. Chulkov, *Scientific Reports* **5** (2015), ISSN 2045-2322, URL <http://www.nature.com/articles/srep12819>. II, III
- [38] S. V. Eremeev, G. Landolt, T. V. Menshchikova, B. Slomski, Y. M. Koroteev, Z. S. Aliev, M. B. Babanly, J. Henk, A. Ernst, L. Patthey, et al., *Nature Communications* **3**, 635 (2012), ISSN 2041-1723. II
- [39] A. M. Shikin, D. A. Estyunin, N. L. Zaitsev, D. Glazkova, I. I. Klimovskikh, S. O. Filnov, A. G. Rybkin, E. F. Schwier, S. Kumar, A. Kimura, et al., *Phys. Rev. B* **104**, 115168 (2021), publisher: American Physical Society, URL <https://link.aps.org/doi/10.1103/PhysRevB.104.115168>. II, III, III
- [40] N. L. Zaitsev, R. Tonner, and I. A. Nechaev, *J. Phys.: Condens. Matter* **31**, 204001 (2019), ISSN 0953-8984. III, III
- [41] S. V. Eremeev, M. G. Vergniory, T. V. Menshchikova, A. A. Shaposhnikov, and E. V. Chulkov, *New Journal of Physics* **14**, 113030 (2012). III
- [42] D. Pacilè, S. V. Eremeev, M. Caputo, M. Pisarra, O. De Luca, I. Grimaldi, J. Fujii, Z. S. Aliev, M. B. Babanly, I. Vobornik, et al., *physica status solidi (RRL) – Rapid Research Letters* **12**, 1800341 (2018).
- [43] A. M. Shikin, D. A. Estyunin, I. I. Klimovskikh, S. O. Filnov, E. F. Schwier, S. Kumar, K. Miyamoto, T. Okuda,

- A. Kimura, K. Kuroda, et al., *Scientific Reports* **10**, 13226 (2020), ISSN 2045-2322. III
- [44] L. Chen, M. Gmitra, M. Vogel, R. Islinger, M. Kronseder, D. Schuh, D. Bougeard, J. Fabian, D. Weiss, and C. H. Back, *Nat. Electron.* **1**, 350 (2018), ISSN 2520-1131, URL <https://www.webofscience.com/wos/woscc/full-record/WOS:000444077900011>. III
- [45] W. Lin, L. Li, F. Doğan, C. Li, H. Rotella, X. Yu, B. Zhang, Y. Li, W. S. Lew, S. Wang, et al., *Nat Commun* **10**, 3052 (2019), ISSN 2041-1723, URL <https://www.nature.com/articles/s41467-019-10961-z>.
- [46] D. Maryenko, M. Kawamura, A. Ernst, V. K. Dugaev, E. Y. Sherman, M. Kriener, M. S. Bahramy, Y. Kozuka, and M. Kawasaki, *Nat Commun* **12**, 3180 (2021), ISSN 2041-1723, URL <https://www.nature.com/articles/s41467-021-23483-4>. III
- [47] X.-L. Qi, T. L. Hughes, and S.-C. Zhang, *Phys. Rev. B* **78**, 195424 (2008). III
- [48] M. Mogi, T. Nakajima, V. Ukleev, A. Tsukazaki, R. Yoshimi, M. Kawamura, K. S. Takahashi, T. Hanashima, K. Kakurai, T. H. Arima, et al., *Phys. Rev. Lett.* **123**, 016804 (2019). III
- [49] Y. Deng, Y. Yu, M. Z. Shi, Z. Guo, Z. Xu, J. Wang, X. H. Chen, and Y. Zhang, *Science* **367**, 895 (2020). III
- [50] J. Wang, B. Lian, X.-L. Qi, and S.-C. Zhang, *Phys. Rev. B* **92**, 081107(R) (2015). III
- [51] H.-G. Zirnstein and B. Rosenow, *physica status solidi (b)* **257**, 1900698 (2020). III
- [52] L. Fu, *Phys. Rev. Lett.* **103**, 266801 (2009), URL <https://link.aps.org/doi/10.1103/PhysRevLett.103.266801>. III
- [53] V. K. Dugaev, P. Bruno, M. Taillefumier, B. Canals, and C. Lacroix, *Phys. Rev. B* **71**, 224423 (2005), URL <https://link.aps.org/doi/10.1103/PhysRevB.71.224423>. IV
- [54] S. Onoda, N. Sugimoto, and N. Nagaosa, *Phys. Rev. Lett.* **97**, 126602 (2006), URL <https://link.aps.org/doi/10.1103/PhysRevLett.97.126602>.
- [55] I. A. Ado, I. A. Dmitriev, P. M. Ostrovsky, and M. Titov, *Phys. Rev. Lett.* **117**, 046601 (2016), URL <https://link.aps.org/doi/10.1103/PhysRevLett.117.046601>. IV
- [56] M. Trushin, K. Výborný, P. Moraczewski, A. A. Kovalev, J. Schliemann, and T. Jungwirth, *Phys. Rev. B* **80**, 134405 (2009), URL <https://link.aps.org/doi/10.1103/PhysRevB.80.134405>. IV
- [57] N. Wadehra, R. Tomar, R. M. Varma, R. K. Gopal, Y. Singh, S. Dattagupta, and S. Chakraverty, *Nature Communications* **11**, 874 (2020), ISSN 2041-1723, URL <https://doi.org/10.1038/s41467-020-14689-z>. IV
- [58] P. M. Sass, J. Kim, D. Vanderbilt, J. Yan, and W. Wu, *Phys. Rev. Lett.* **125**, 037201 (2020). IV
- [59] A. Fedorov, Y. V. Pershin, and C. Piermarocchi, *Phys. Rev. B* **72**, 245327 (2005), URL <https://link.aps.org/doi/10.1103/PhysRevB.72.245327>. IV
- [60] Y. V. Pershin and C. Piermarocchi, *Applied Physics Letters* **86**, 212107 (2005).
- [61] N. Ogawa, R. Yoshimi, K. Yasuda, A. Tsukazaki, M. Kawasaki, and Y. Tokura, *Nature Communications* **7**, 12246 (2016), ISSN 2041-1723, URL <https://doi.org/10.1038/ncomms12246>. IV
- [62] D. Bang, H. Awano, J. Tominaga, A. V. Kolobov, P. Fons, Y. Saito, K. Makino, T. Nakano, M. Hase, Y. Takagaki, et al., *Scientific Reports* **4**, 5727 (2014), ISSN 2045-2322, URL <https://doi.org/10.1038/srep05727>. IV
- [63] M. Buchner, P. Högl, S. Putz, M. Gmitra, S. Günther, M. A. W. Schoen, M. Kronseder, D. Schuh, D. Bougeard, J. Fabian, et al., *Phys. Rev. Lett.* **117**, 157202 (2016). IV
- [64] M. Sato, Y. Takahashi, and S. Fujimoto, *Phys. Rev. Lett.* **103**, 020401 (2009). IV
- [65] M. Sato and S. Fujimoto, *Phys. Rev. B* **79**, 094504 (2009). IV